

Probing hypernuclei at PANDA and at MAMI-C*

P. Achenbach

Institut für Kernphysik, Johannes Gutenberg-Universität, D-55099 Mainz, Germany.

Società Italiana di Fisica / Springer-Verlag 2007

Abstract. Spectroscopy of Λ hypernuclei has recently become one of the most valuable tools for the experimental investigation of strangeness nuclear physics. Several new approaches are being pursued currently: In Mainz, the Microtron MAMI has been upgraded to 1.5 GeV electron beam energy and will be used to produce strange hadronic systems in the near future. The KaoS spectrometer is being installed for large acceptance, high resolution strangeness reaction spectroscopy at the existing spectrometer facility. The Mainz hypernuclei research programme will be complemented by experiments on multi-strange systems at the planned FAIR facility at GSI. The γ -ray spectroscopy of double Λ hypernuclei produced via $\Xi\bar{\Xi}$ pair production is one of the four main topics which will be addressed by the PANDA Collaboration. In this paper the status of the planned experiments and the future prospects are presented.

PACS. 21.80.+a Hypernuclei – 25.30.Rw Electroproduction reactions – 25.43.+t Antiproton-induced reactions – 07.05.Fb Design of experiments – 07.05.Hd Data acquisition: hardware and software

1 Introduction

Open strangeness production is undergoing a renewed interest, both theoretically and experimentally. On the theoretical side, due to the non-perturbative nature of Quantum Chromodynamics (QCD) at low energies, strange systems cannot be described by the fundamental equations for the dynamics of (asymptotically free) quarks and gluons. Instead, isobaric models are commonly used in kaon production, where the hadrons are treated as effective degrees of freedom. The partonic constituents can also be considered along the lines of chiral models, which take the chiral symmetry of the QCD Lagrangian and its spontaneous breakdown into account. Although lattice QCD calculations are not yet relevant to kaon production, it is anticipated that precise experimental data on strangeness production will challenge and improve our understanding of the strong interaction in the low energy regime of QCD. Since direct scattering experiments with hyperons are impractical, the spectroscopy of hypernuclei provides a unique approach to explore the baryon-baryon interaction. This field of physics will be addressed by the Mainz Microtron MAMI, recently upgraded to 1.5 GeV electron beam energy and at the antiproton storage ring HESR of the future FAIR facility at GSI.

The (K^-, π^-) reaction is characterised by the existence of a "magic momentum" where the recoil momentum of the hyperon essentially becomes zero. It populates,

consequently, substitutional states in which a nucleon is converted to a hyperon in the same orbital state. The (e, e', K^+) reaction, in contrast, produces hypernuclei by converting a proton into a hyperon and transfers a large momentum to a hypernucleus. The electroproduction process has the unique characteristic of providing large amplitudes for the population of spin-flip hypernuclear states with unnatural parities [1].

In the case of the ΛN strong potential, the spin-orbit term is known to be much smaller than in NN interaction. Although these transitions can only be observed using γ -spectroscopy [2], reaction spectra are equally important because they provide the complete spectrum of excitations with a strength that not only gives the spectroscopic factor, but the transition matrix. A deeper understanding of the Λ potential relies on obtaining high quality data for hypernuclei. The present experimental data on binding energies and detailed spectroscopic features are limited in quantity and quality and refer mostly to light (s - and p -shell) hypernuclei.

2 Production of hypernuclei at MAMI-C

Electron beams have excellent spatial and energy definitions, and targets can be physically small and thin ($10-50$ mg/cm²) allowing studies of almost any isotope. The small cross section for the reaction, $\sigma \sim 140$ nb/sr on a ¹²C target [3], compared to strangeness exchange $n(K^-, \pi^-)\Lambda$ or to associated production $n(\pi^+, K^+)\Lambda$ is well compensated by the available high electron beam intensities. Even though an increasing number of new experiments are now

* Supported by the Bundesministerium für Bildung und Forschung (bmb+f) under contract no. 06MZ176 and by the EU integrated infrastructure initiative HadronPhysics project under contract no. RII3-CT-2004-506078.

being performed in hypernuclear spectroscopy, our knowledge on hypernuclei is still limited to a small number of isotopes. With the commissioning of the 1.5 GeV electron beam of MAMI-C the study of hypernuclei has become possible in Mainz.

In electroproduction the angular distribution of kaons associated with a given hypernuclear state is sensitive to the Λ wave function inside the nucleus [4,5]. A hypernuclear Λ samples the nuclear core where there is little direct information on the single particle structure. In addition, high resolution spectroscopic studies of hypernuclei can be performed in order to provide the most valuable experimental information on the Λ dynamics in nuclei.

One of the factors decisive for the feasibility of an experiment at MAMI is of course the reaction rate. To optimise the reaction rate the hypernuclear formation in impulse approximation was modelled. In order to form a hypernucleus, the hyperon produced in the reaction has to be bound by the core nucleus. The transition form factor depends very much on the transferred momentum to the hyperon. If the momentum transfer is large compared with typical nuclear Fermi momenta, the hyperon will emerge from the nucleus.

Assuming 3-momentum conservation at the vertices of the Feynman diagram in impulse approximation the transferred momentum can be written as the difference between Λ momentum, \mathbf{p}_Λ , and core nucleus momentum, \mathbf{p}_{A-1} , and is a function of the momentum of the virtual proton, \mathbf{k} , and the recoil momentum of the hypernucleus, \mathbf{p}_Y : $q(k) \equiv |\mathbf{p}_\Lambda - \mathbf{p}_{A-1}| = |\mathbf{p}_Y + 2\mathbf{k}|$. For the kinematical optimisation an approximate Fermi Gas distribution for the virtual proton, $F = 2\pi \int_0^\infty n(k)k^2 dk$ was assumed, where the distribution function, $n(k)$, is Gaussian, $n(k) = (2^{-4}k_F\sqrt{\pi})^{-3} \exp -\sqrt{2}k^2/k_F^2$. By modelling the transition form factor with an exponential function, $S_\Lambda = \iint \exp(-q(k)/\sigma_p)n(k)k^2 dk d\cos\theta$, it can be evaluated as a function of the kinematic variables. Since electroproduction is a high momentum transfer reaction similar to (π^+, K^+) , the transition form factor takes a minimum at threshold and increases as the virtual photon energy increases. An interpretation of the transition form factor in terms of a sticking probability is given, for example, in [6], for the case of harmonic oscillator wave functions. Using this interpretation the sticking probability prevails at low q and substitutional states are exclusively populated, whereas at $q \sim k_F$, high quantum numbers and spin stretched states are favoured.

The cross section for electroproduction can be written in a very intuitive form by separating out a factor, Γ , which multiplies the off-shell (virtual) photoproduction cross sections. This factor may be interpreted as the flux of the virtual photon field per scattered electron into $dE'd\Omega$ and can be written as $\Gamma = \frac{\alpha}{2\pi^2} \frac{E'}{E} \frac{k_\gamma}{Q^2} \frac{1}{1-\epsilon}$, with $k_\gamma = (W^2 - m_i^2)/2m_i$ and $\epsilon = (1 + 2\frac{|\mathbf{q}|^2 \tan^2 \frac{\theta}{2}}{Q^2})^{-1}$, where \mathbf{q} is the virtual photon three-momentum. The virtual photon flux factor has the feature that it is very forward peaked. While the flux factor for a fixed photon energy, $\omega = E_e - E'_e$, increases with beam energy, so does the mass resolution and the background rate. In Fig. 1 the electron

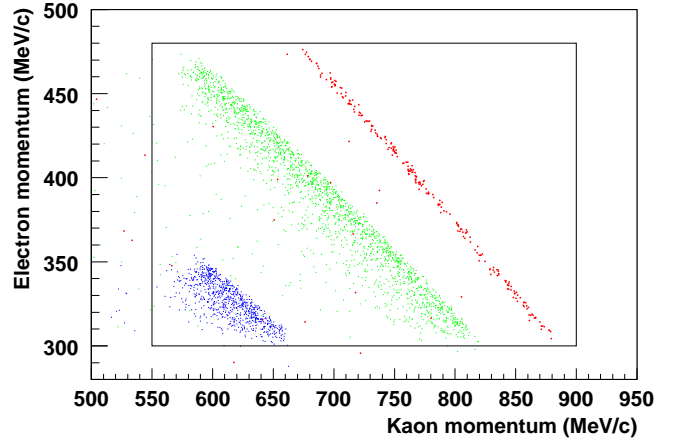


Fig. 1. Simulated correlation between electron and kaon momenta, where Λ (green) and Σ (blue) hyperons have been generated for the elementary production off the proton and the $^{12}_\Lambda\text{B}$ hypernuclei (red) have been generated in a carbon target. The rectangular box indicates the acceptance of KaoS.

momentum is plotted versus the kaon momentum, where Λ and Σ hyperons have been generated for the elementary production off the proton and the $^{12}_\Lambda\text{B}$ hypernuclei have been generated in a carbon target. The events have been generated randomly in phase-space and weighted by a factor for the virtual photon flux and the modelled transition form factor. In the Monte Carlo, the production probability was assumed to drop exponentially with the relative momentum between Λ and core nucleus and typical values of $\sigma_p = 100 \text{ MeV}/c$ and $k_F = 200 \text{ MeV}/c$ were assumed. The proposed kinematic setting for a first hypernuclear formation experiment has been defined accordingly. From the acceptance at a magnetic field setting of 1.1 T a scattered electron energy of 400 MeV at a scattering angle of 3° was chosen, resulting in 1100 MeV photon energy. This correlates to a kaon momentum of about 760 MeV/c.

2.1 The KaoS spectrometer

Experimentally, the conservation of strangeness in electromagnetic and strong interactions allows the tagging of baryonic systems with open strangeness, e.g. baryon resonances or hypernuclei, by detecting a kaon in the final channel.

KaoS is a very compact magnetic spectrometer suitable especially for the detection of kaons. It was built for the GSI for heavy ion induced experiments [7]. During May and June 2003 the spectrometer was brought to Mainz. A graphical visualisation of KaoS at its future measurement position close to the target in the spectrometer hall is given in Fig. 2. As a pilot experiment on kaon electroproduction, the separation of transverse and longitudinal structure functions in parallel kinematics is planned with the available detector package [8]. The use of KaoS as a two arm spectrometer for the electroproduction of hypernuclei at MAMI requires the detection of the scattered

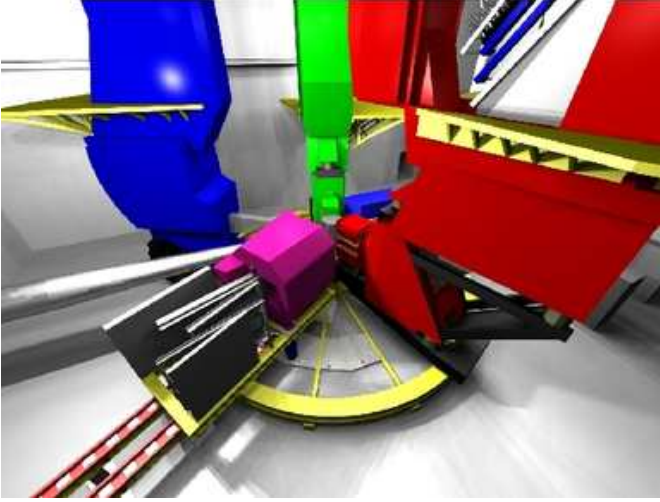


Fig. 2. Graphical visualisation of KaoS at its measurement position close to the target in the spectrometer hall.

electron at laboratory angles close to 0° . The kaon detector in the focal plane has to cover a wide range of scattering angles around 5° in coincidence to the electron detection. In order to cope with the kinematical situation in electroproduction of hypernuclei and with the high background rates, KaoS will be equipped with new read-out electronics, a completely new focal plane detector package for the electron arm, and a new trigger system.

2.2 Development of Detectors

The main focal plane detector of the KaoS electron arm will mainly consist of 2 horizontal planes of fibre arrays, covering an active area of $1780 \times 300 \text{ mm}^2$, and comprising ~ 2000 channels per plane. Each plane is divided into detector segments which consist of 384 fibres in three joined fibre bundles coupled to three multi-anode photomultipliers (MaPMTs) mounted on a single 96-channel front-end board, see Fig. 3 for a photograph.

A fibre doublet structure is formed from two single layers of fibres, with one of the fibre layers off-set relative to the other by half a fibre spacing. The virtue of this configuration is the high fraction of overlapping fibres, i.e. a high detection efficiency, and a small pitch leading to a good spatial resolution. Two of such double layers are placed together in the focal plane detector to increase its efficiency.

The fibres are of type Kuraray SCSF-78 with a double cladding of 0.83 mm outer diameter. The total cladding thickness is 0.1 mm, leading to a 0.73 mm core of refractive index $n_{\text{core}} = 1.6$. Four fibres are grouped to one channel and brought to one pixel of the photo-tubes of type R7259K from Hamamatsu with a 32-channel linear array of anodes. The photocathode material is bi-alkali and the window is made of 1.5 mm thick borosilicate glass. The effective area per channel is $0.8 \times 7 \text{ mm}^2$ with a pitch of 1 mm.

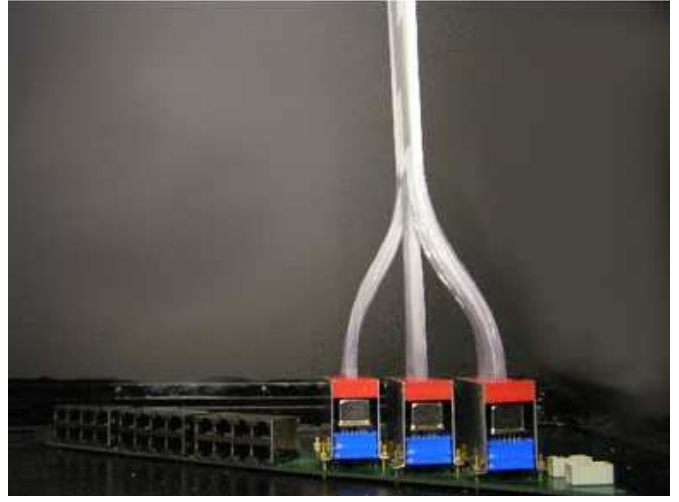


Fig. 3. Photograph of a detector with three joined fibre bundles and three MaPMTs mounted on a single front-end board.

Instead of supplying dynode voltages through a voltage divider, the MaPMTs are powered by individual Cockcroft-Walton bases, manufactured by HVSystems, Dubna. The dc voltage is pulsed and converted with a voltage doubler ladder network of capacitors and diodes to higher voltages. The principal advantage is that there is no need for stiff high voltage cables, since only $\sim 140 \text{ V}$ has to be delivered to the first front-end board, where the voltage is daisy-chained to the other boards of the detector plane. One drawback is that the inter-dynode voltages can only be equally spaced, which is acceptable for their actual use.

Since the scattered electrons have an inclination angle of $50 - 70^\circ$ with respect to the normal of the focal plane a configuration with hexagonal fibre packing has been chosen. This packing, in which each fibre is surrounded by 6 other fibres, has the highest possible density of $\frac{\pi}{\sqrt{12}} \simeq 0.9$. The main consequence of the incident angle distribution is an increased channel multiplicity. The amount of scattering depends primarily on the momentum and the effective thickness of the scattering medium (radiation length $X_0 = 42 \text{ cm}$ for polystyrene). Electron trajectories for different momenta cross the focal plane detector at different positions under slightly different angles. The average thickness and its variation was simulated for to be $x = (4.7 \pm 1.3) \text{ mm}$. This number translates into an rms width of $\theta_0 = 0.23^\circ$ for $p = 300 \text{ MeV}/c$. The main consequence of the incident angle distribution is an increased channel multiplicity.

2.3 Development of Electronics

A 32-channel discriminator board with 4 integrated low-walk double threshold discriminators (DTDs) for amplitude compensated timing was built, see Fig. 5 (left) for a photograph of the DTD board. The detectors are connected to the board by RJ-45 cables (with 4 channels per cable). The DTD boards have two multiplexed coaxial

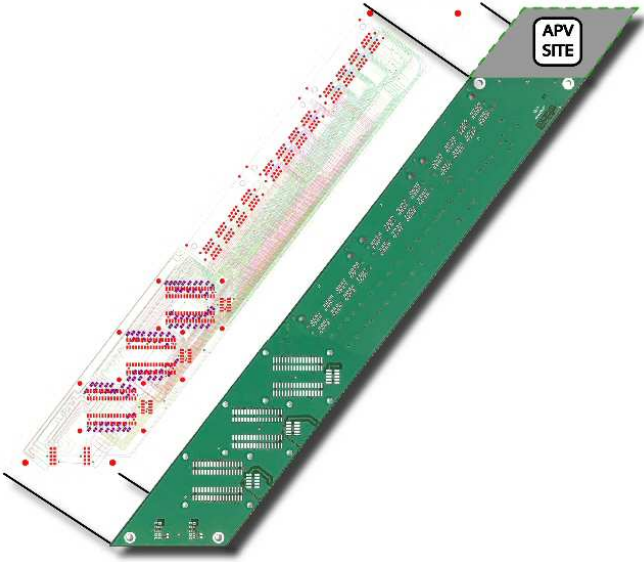


Fig. 4. Photograph and circuit scheme of the triple front-end board showing the three MaPMT sockets at the lower left, and the output sockets. The site for the APV chip connector is indicated.

$50\ \Omega$ analogue outputs for debugging and two LVDS outputs, one to be connected to TDC modules, and one to the trigger modules. A 32-channel analogue output board can be attached to the discriminator board for a complete analysis of analogue signals. Up to 20 DTD boards fit into a VME 6U crate together with a controller board, see Fig. 5 (right) for a photograph.

Time measurements are performed with an electronic system based on CATCH, the COMPASS Accumulate, Transfer and Control Hardware system from the COMPASS experiment at CERN [9]. Each CATCH module is equipped with 4 TDC mezzanine cards with 32 read-out channels per card. The CATCH module not only serves as an interface between front-end electronics and the data taking processor, but also acts as an integral part of the trigger distribution and time synchronisation system (TCS). At the heart of a mezzanine card is the so-called $\mathcal{F}1$ chip with 8 channels of ~ 120 ps resolution (LSB) each. The tracking trigger will be derived with VME Universal Processing Modules. Such a module is equipped with one 500 MHz FPGA, one 1 GHz DSP, and 256 LVDS inputs or outputs.

In addition to timing and trigger, an analogue signal read-out system capable of handling high channel counts is also needed. For this purpose, the APV chip and the GeSiCa data collector card of the COMPASS electronics is under investigation. The APV chip acts as an analogue ring-buffer at 40 MHz, which on demand multiplexes the appropriate 128-channel sample and sends it to an attached ADC. The GeSiCa module provides the TCS information processing, data collection, data concentration and data transfer to PC-based read-out buffer cards via SLink.



Fig. 5. Left: photograph of the double threshold discriminator board. The two LVDS outputs are visible near the bottom of the module. The RJ-45 inputs are located at the top left of the module and the two coaxial $50\ \Omega$ outputs at centre left. Right: photograph of the controller board for up to 20 double threshold discriminator boards.

2.4 Performance of Detectors and Electronics

After a first characterisation of several detector prototypes [10], a triple detector with 96 read-out channels for three fibre bundles was tested in Cave C of GSI with a ^{12}C beam of 2 AGeV energy provided by SIS18. In each bundle 128 fibres were packed in 4 double layers with a pitch of 0.6 mm. Two bundles were aligned to a single plane perpendicular to the beam, and one bundle formed a parallel plane directly behind.

In deducing the time resolution clusters of correlated hit times were searched for. The cluster with the time closest to the trigger signal time was retained, and within the cluster the time of the first arrived signal was chosen as hit time. The hit time residual, defined as the difference between the two hit times in the two planes of fibres, was distributed with a FWHM of 330 ps as shown in Fig. 6. The time resolution of a single detector plane was determined to be of the order of $\text{FWHM} \sim 330\ \text{ps}/\sqrt{2} = 230$ ps.

Cross-talk in the MaPMT entrance window perturbed the reconstruction of the particle position. By using the pulse height information the hit channel was estimated by the centroid of charges of up to 5 neighbouring channels. The hit position residual, defined as the difference between the two estimates in the two planes of fibres, had a FWHM of 0.27 mm as shown in Fig. 7, although the estimator contained a spatial digitalisation error. The achieved accuracy was sufficient for an unambiguous identification of the hit channel leading to a spatial accuracy of $0.6\ \text{mm}/\sqrt{12} \approx 170\ \mu\text{m}$ (rms).

2.5 Perspective

The special kinematics for electroproduction of hypernuclei requires the detection of both, the associated kaon and the scattered electron, at forward laboratory angles.

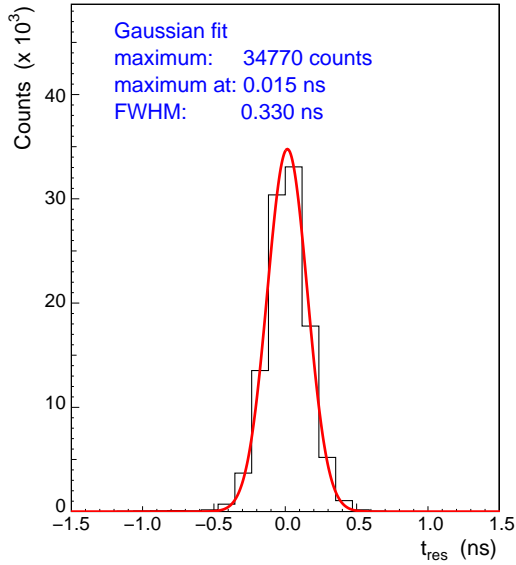


Fig. 6. The residual of hit times between both detector planes. A Gaussian fit is shown with a FWHM of 330 ps.

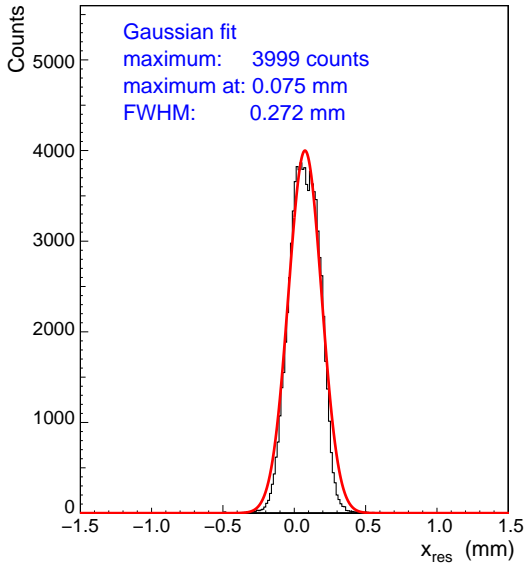


Fig. 7. The residual of beam position estimates between both detector planes, using the centroid of charges. A Gaussian fit is shown with a FWHM of 0.27 mm.

While the scattered electrons have to be detected at very forward angles, the kaon detector has to cover a broader range of up to 15° in order to extract dynamical information from the K^+ angular distribution. The potential of electroproduction at MAMI-C is an energy resolution of a few hundred keV with reasonable counting rates up to at least medium weight hypernuclei. An important goal for measuring the excitation spectra and decay properties of strange hypernuclei is to test the energies and wave functions from microscopic structure models and to put constraints on baryon-baryon interaction models.

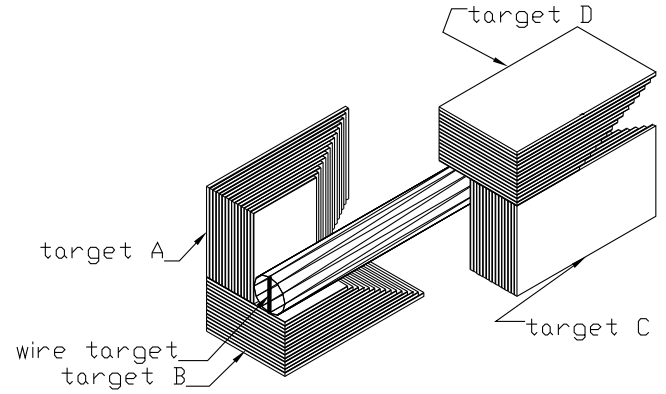


Fig. 8. Exploded view of the target region showing the wire target, the beam-line, and the sandwich structure of silicon layers with a combination of target materials (A–D).

3 Hypernuclear γ -spectroscopy with $\overline{\text{PANDA}}$

At FAIR a new technique for producing double hypernuclei with antiprotons will be pursued. Their study will reveal the $\Lambda\Lambda$ strong interaction strength, not feasible with direct scattering experiments. $\overline{\text{PANDA}}$ will also contribute to the intensive search for the H dibaryon composed of two u, d, and s quarks, producing a deeply bound system.

At the antiproton beam relatively low momentum Ξ^- can be produced in $\overline{p}p \rightarrow \Xi^- \overline{\Xi}^+$ or $\overline{p}n \rightarrow \Xi^- \overline{\Xi}^0$ reactions [11]. The advantages as compared to the kaon induced reactions are (i) the retainment of the antiproton beam in a storage ring, (ii) the presence of the $\overline{\Xi}$ antiparticle, that will be used to tag the strangeness in the reaction, and (iii) the high production rate with respect to the annihilation of antiprotons at rest with subsequent strangeness exchange. This allows a rather high luminosity even with very thin primary targets.

The associated $\overline{\Xi}$ will undergo scattering or (in most cases) annihilation inside the residual nucleus and a trigger can be based on the detection of the surviving anti-hyperons under small angles. Since strangeness is conserved in the strong interaction and the annihilation products contain at least two anti-kaons, an alternative tag for the reaction can be based on the detection of positive kaons with relatively low momentum in $\overline{\text{PANDA}}$.

The slowing down the Ξ^- proceeds (i) through a sequence of nuclear elastic scattering events inside the residual nucleus in which the annihilation has occurred and (ii) by energy loss during the passage through an active absorber. If decelerated to rest before decaying, the particle can be captured inside a nucleus, eventually releasing two Λ hyperons and forming a double hypernuclei. In Fig. 8 the geometry of the secondary target is shown, where the radial dimension was determined by the short life-time of the Ξ^- particle while the angular coverage is limited by the kaon detection in forward direction, making use of the tracking probability of the general purpose $\overline{\text{PANDA}}$ set-up. The integration of the hypernuclear physics set-up into $\overline{\text{PANDA}}$ is shown in Fig. 9. The absorber will consist of a sandwich structure of silicon layers and a combination

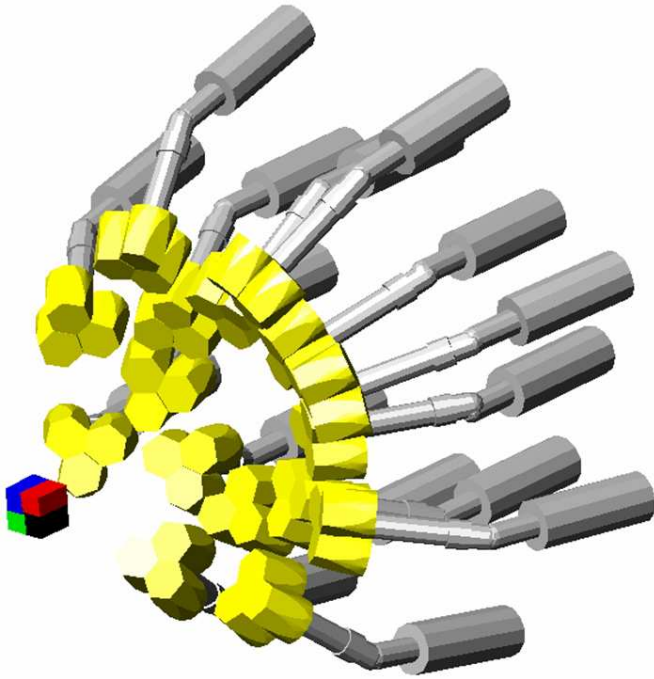


Fig. 9. Hypernuclear physics set-up showing (i) the secondary target, and (ii) the cluster detectors, each consisting of 3 hexagonal HPGe crystals packed in a common cryostat and an electromechanical cooler.

of target materials. The choice of the target is crucial for the magnitude of the cross section. Also the number of excited states of the core should be small and the states should be well separated.

The level scheme of single and double hypernuclei will be explored by γ -ray detection. Only recently, high resolution spectroscopy of hypernuclei with germanium arrays was established. Spectroscopic information on double hypernuclei can only be obtained via their sequential decays. To maximise the detection efficiency the high purity germanium (HPGe) detectors have to be located near the target, and thus have to be operated in a strong magnetic field. In combination with the high luminosity of the HESR machine at FAIR and with the proposed solid-state micro-tracker, high resolution γ -ray spectroscopy of double hypernuclei will become possible for the first time.

The multiple steps in the production and detection chain of double hypernuclei have been discussed in Ref. [12]. One of the unknown factors in the realization of the experiment is the performance of HPGe detectors in strong magnetic fields. To verify that HPGe detectors can be safely and efficiently operated in such an environment two different kind of detectors have been tested in the field provided by the ALADiN magnet at GSI: the Euroball cluster detector [13] and the VEGA detector [14]. A small degradation of the energy resolution was found, and a change in the rise time distribution of the preamplifier pulses was observed [15]. Fig. 10 shows the energy resolution (FWHM) at 1.333 MeV of one channel of each detector as a function of the magnetic field. A correlation between rise time and pulse height is used to correct the measured energy,

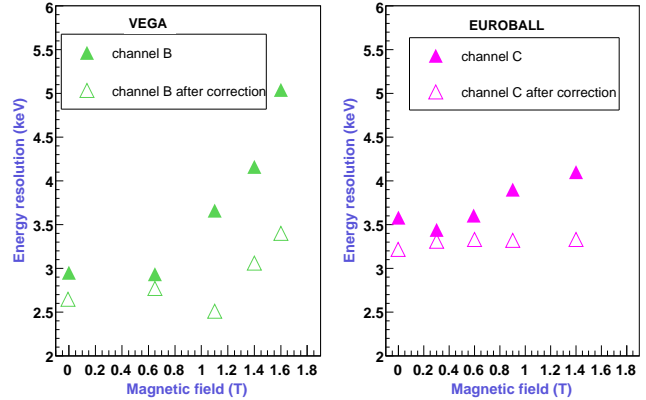


Fig. 10. Measured energy resolution (FWHM) for the 1.333 MeV γ -line of Euroball cluster and VEGA detectors in a magnetic field with and without correction [16]. Statistical errors for the values are smaller than the symbol size.

recovering the initial energy resolution almost completely. This promising result offers the opportunity not only for hypernuclear γ -spectroscopy with PANDA, but also for a possible FINUDA spectrometer up-grade at DAΦNE [17].

References

1. T. Motoba, M. Sotona, and K. Itonaga, *Prog. Theor. Phys. Suppl.* **117**, (1994) 123.
2. H. Tamura et al., *Nucl. Phys.* **A754**, (2005) 58.
3. T. Miyoshi et al., *Phys. Rev. Lett.* **90**, (2003) 232502.
4. S. Shimamura, *Prog. Theor. Phys.* **92**, (1994) 571.
5. C. Bennhold et al., *nuc1-th/0011022*, 1999.
6. H. Bando, T. Motoba, and J. Žofka, *Int. J. Mod. Phys.* **A5**, (1990) 4021.
7. P. Senger et al. (KaoS Collab.), *Nucl. Instr. and Meth.* **A327**, (1993) 393.
8. P. Achenbach et al. (A1 Collab.), accepted proposal MAMI-A1/1-03 (Inst. für Kernphysik, Mainz 2003).
9. P. Abbon et al., *Nucl. Instr. and Meth. A* (2007), in Press.
10. P. Achenbach et al., *New detectors for the kaon and hypernuclear experiments with KaoS at MAMI and with PANDA at GSI*, in Proc. of the IX. Intern. Symposium on Detectors for Particle, Astroparticle and Synchrotron Radiation Experiments, SLAC, 3–6 April 2006, ed. by V. Luth (2006).
11. PANDA Collab., *Technical progress report for PANDA: strong interaction studies with antiprotons* (GSI, Darmstadt 2005).
12. J. Pochodzalla, *Nucl. Instr. and Meth.* **B214**, (2004) 149.
13. J. Eberth et al., *Nucl. Instr. and Meth.* **A369**, (1996) 135.
14. J. Gerl et al., in: Proc. Conf. on Physics from Large γ -ray Detector Arrays, Berkeley, LBL Report 35687, (1994) 159.
15. A. Sanchez Lorente et al. (HyperGamma Collab.), *Nucl. Instr. and Meth.* **A573**, (2007) 410.
16. A. Sanchez Lorente, *Seminar at the Institut für Kernphysik, Joh. Gutenberg-Univ., Mainz*, Jan. 2007.
17. A. Feliciello, this conference.